Applied Catalysis B: Environmental 325 (2023) 122328

Contents lists available at ScienceDirect

Applied Catalysis B: Environmental

journal homepage: www.elsevier.com/locate/apcatb

Surface compositional dynamics in a PtNi bimetallic alloy under simulated operational conditions: Electrochemical and NAP-XPS Study

Xianxian Xie, Athira Lekshmi Mohandas Sandhya, Lesia Piliai, Mykhailo Vorokhta, Iva Matolínová, Ivan Khalakhan *

Charles University, Faculty of Mathematics and Physics, Department of Surface and Plasma Science, V Holešovičkách 2, Prague 180008, Czech Republic

ARTICLE INFO

Keywords:
Alloys
Surface chemistry
Electrochemistry
Photoelectron spectroscopy
Cyclic voltammetry

ABSTRACT

Platinum-based bimetallic alloys possess unique activities exceeding those of pure platinum. Nevertheless, as complex multi-component systems, they suffer from surface structural reorganization under operating conditions, strongly affecting their lifetime performance. This work reports an *in situ* electrochemical and spectroscopic study of surface compositional changes in a PtNi catalyst during repetitive oxidation/reduction cycles, simulating inherent working conditions for numerous redox reactions. Using cyclic voltammetry and near-ambient pressure X-ray photoelectron spectroscopy, quantitative surface characterization under realistic electrified liquid and gaseous environments are obtained and correlated. We show that regardless of the operating environment, PtNi undergoes a significant and irreversible change in compositional profile reflected in surface nickel enrichment and consequent catalyst deactivation, exemplary confirmed using a methanol electrooxidation reaction.

1. Introduction

Bimetallic catalysts are of great interest nowadays due to their wide range of applications [1]. Given their distinctive merits, such catalysts typically show superior activities in many catalytic reactions compared with their monometallic counterparts, often exhibiting advantages of both. In particular, alloying of Pt with cheaper and more abundant 3d transition metals has been proven beneficial for many reactions, due to both exclusive properties and reduced price. To date, Pt-3d metal catalysts of various compositions have been explored to substitute for typical monometallic catalysts in various reactions including oxygen reduction [2,3], hydrogen evolution [4], methanol oxidation [5,6], ethanol oxidation [7], etc. Their distinctive properties were mainly attributed to the modified electronic structure that displaces the d-band center, resulting in optimum strength with adsorbates thereby increasing reaction rates [8].

On the other hand, bimetallic catalyst falls under complex multi-component systems that typically exhibit composition-dependent activity [9,10]. Specific reaction conditions such as gas pressure, temperature and the nature of reaction intermediates may dramatically compromise the chemical integrity of the alloy surface [11–14]. The surface atomic composition of a bimetallic system under reaction conditions may thus be different from an as-synthesized catalyst, significantly affecting its activity and selectivity [15].

The interdiffusion of constituent elements under reaction conditions is a complex phenomenon driven by the interplay of multiple parameters including surface energies of elements, diffusion barriers, their bonding strength with a given adsorbate, pressure and temperature. For this reason, direct monitoring of bimetallic catalysts under specific working conditions is of utmost importance for the knowledge-based development of highly effective and, more importantly, durable catalysts. A significant step forward has been made in recent years by developing *in situ/operando* techniques capable of probing catalysts directly under reaction conditions [16,17]. Compositional evolutions in response to reaction conditions have been investigated for a wide range of Pt-based bimetallic materials including Pt-Co [18–20], Pt-Ni [21–25], Pt-Cu [26], Pt-Sn [27,28] systems. It has been shown that such restructuring may be either beneficial or detrimental for a given reaction [29,30]. For instance, Ahmadi et al. showed that pretreatment under different gaseous atmospheres significantly affected the catalytic reactivity of shaped $Pt_{0.5}Ni_{0.5}$ nanoparticles toward CO electrooxidation [21]. Mayrhofer et al. reported that CO-annealing pretreatment resulted in Pt atom segregation to the surface of a Pt_3Co alloy, increasing its activity towards oxygen reduction reaction [20]. In a recent study, Wang

* Corresponding author.
E-mail addresses: khalakhan@gmail.com, ivan.khalakhan@mff.cuni.cz (I. Khalakhan).

https://doi.org/10.1016/j.apcatb.2022.122328
Received 12 July 2022; Received in revised form 22 December 2022; Accepted 25 December 2022
Available online 26 December 2022

et al. showed that a Pt_3Sn catalyst can recover its surface composition following reduction during propane dehydrogenation through segregation of the Sn atoms from the bulk once the Sn content at the surface becomes insufficient [27]. On the contrary, Andersson and co-workers found that CO adsorption at elevated pressures and temperatures pulls the less reactive Cu to the surface of a CuPt near-surface alloy [26]. In our previous study using *ex situ* surface sensitive synchrotron radiation photoelectron spectroscopy, we showed that after repetitive exposure to oxygen and hydrogen, the PtNi bimetallic alloy surface composition irreversibly changed towards Ni enrichment [31]. However, a complete deciphering of catalyst working mechanisms requires these systems to be studied under more realistic conditions resembling *operando* regimes more closely. Achieving such a goal requires the application of a limited number of techniques that allow direct quantification of the surface composition of the alloy under environments relevant or identical to the catalytic operation. The most suitable techniques satisfying this goal are cyclic voltammetry (CV) and near-ambient pressure X-ray photoelectron spectroscopy (NAP-XPS). Both are extremely sensitive to surface composition and can be performed directly under electrochemical or gaseous environments [10,11,20,24,32].

In the present work, we report a combined *in situ* electrochemical and spectroscopic study of surface structural changes in a PtNi catalyst during repetitive oxidation and reduction, representing inherent working conditions for numerous catalytic redox reactions. The model PtNi catalyst was prepared by magnetron sputtering deposition in the form of compact layers with homogeneous grain-size distribution and high-angle grain boundaries resembling both extended 2D surfaces and the nanoparticle catalyst [33,34]. The repetitive oxidation and reduction of the PtNi catalyst were carried out in both electrified liquid environment and gaseous environment at 100 and 250 °C by applying potentiodynamic cycling in 0.1 M KOH solution and altering sample exposure to 5 mbar of O_2 and H_2, respectively. The resulting restructuring of the alloy surface was monitored by cyclic voltammetry and NAP-XPS.

2. Experimental

2.1. Sample preparation

PtNi alloys were deposited on glassy carbon (GC) substrates (Alfa Aesar) by magnetron co-sputtering using Circular TORUS magnetrons (Kurt J. Lesker) placed at an angle of 45° to the substrate and two targets: 2" Pt (99.99% Safina) and 2" Ni (99.99% Kurt J. Lesker). The sputtering was carried out in 5×10^{-3} mbar of Ar atmosphere in DC mode by applying 20 W to Pt and 28 W to Ni targets, resulting in deposition of the $Pt_{50}Ni_{50}$ layer. The reference monometallic Pt and Ni layers were deposited under identical conditions. The reference NiO layer was deposited in 5×10^{-3} mbar of O_2 atmosphere. The thickness of all investigated catalytic layers was about 10 nm.

2.2. Sample characterization

2.2.1. Near-ambient pressure X-ray photoelectron spectroscopy

The experiment was performed using a laboratory NAP-XPS system (SPECS Surface Nano Analysis, GmbH Germany) with "chamber-in-chamber" design. The setup consisted of a main ultra-high vacuum (UHV) analysis chamber equipped with a monochromated Al Kα X-ray source (1486.6 eV), a multichannel electron energy analyzer (SPECS Phoibos 150) coupled with a differentially pumped electrostatic pre-lens system, a port fitted with gate valve separating the analysis chamber, and a NAP cell installed on a special NAP cell manipulator in a different UHV in situ-load-lock chamber. The base pressure in both analysis and load-lock chambers was in the 10^{-9} mbar range. For the NAP-XPS measurements, the gate valve separating the chambers was opened and the NAP cell was brought into the analysis chamber and docked at the entrance aperture of the electron energy analyzer. A sample holder was heated through contact with the hot sample stage heated by electron bombardment from the back (UHV) side. The PtNi sample was measured under atmospheres of 5 mbar of O_2 or 5 mbar of H_2 at a temperature of 100 and 250 °C. The measured Pt 4f, Ni 3p, Ni 2p, and O 1 s core-level spectra were processed using the KolXPD software [35].

2.2.2. Cyclic voltammetry

Cyclic voltammetry was performed in N_2-purged 0.1 M KOH and 0.1 M KOH + 0.5 M CH_3OH solutions at sweep rates of 200 $mV{\cdot}s^{-1}$ and 50 $mV{\cdot}s^{-1}$, respectively, in a typical 3-electrode half-cell (Pine research) using a sample as a working electrode, platinum wire as a counter electrode (Pine research), and Hg/Hg_2SO_4 (Monokrystaly s.r.o.) as a reference electrode. The system was connected to an SP-150 potentiostat (Bio-Logic). The measured potentials vs. the reference Hg/Hg_2SO_4 electrode were converted to the reversible hydrogen electrode (RHE) scale for a more straightforward comparison with the literature. For cyclic voltammetry, Pt and PtNi catalysts were deposited on a commercial glassy carbon disk electrode (Pine research, 5 mm diameter, 0.196 cm^2 surface area). Electrochemical cleaning of deposited PtNi catalysts was carried out in 0.1 M H_2SO_4 for 30 s without applying potential. Data were processed using the EC-lab software (Bio-Logic).

2.2.3. Energy-dispersive X-ray spectroscopy

Energy-dispersive X-ray spectroscopy (EDX) was performed using a Bruker XFlash detector attached to a Tescan MIRA 3 scanning electron microscope.

2.2.4. Atomic force microscopy (AFM)

The morphology of catalysts was examined using a MultiMode 8 (Bruker) Atomic Force Microscope (AFM) in tapping mode under ambient conditions. A SCANASYST-AIR probe (Bruker) with a nominal tip radius of 2 nm was used. Image processing was carried out using NanoScope 1.9 software.

3. Results and discussions

3.1. Cyclic voltammetry study

Cyclic voltammetry was applied to gain insights into compositional changes on the surface of the PtNi bimetallic alloy during its alternating cycles of oxidation and reduction under an electrified liquid environment. Catalyst oxidation and reduction were driven by repetitive potential scanning from low to high values in an electrolyte solution inside an electrochemical cell schematically illustrated in Fig. 1a, together with the applied cycling protocol. Cyclic voltammetry is an extremely surface-sensitive technique that allows semiquantitative information about the composition of the outermost layer of the PtNi alloy to be obtained [10,32,36]. An alkaline solution at pH 13 and a potential range of 0–1 V_{RHE} were chosen to avoid any platinum and nickel dissolution, according to the Pourbaix diagram [37].

Electrochemical cleaning of deposited PtNi catalysts was carried out in 0.1 M H_2SO_4 for 30 s without applying potential. Such a pretreatment led to Ni leaching from the outermost layer of the alloy and the formation of the so-called Pt-skin layer, where PtNi is terminated by Pt atoms only [37–39]. Fig. S1 represents *ex situ* catalyst characterization before and after acid treatment. Only negligible deviation of sample composition was observed after acid treatment, based on the bulk-sensitive EDX in Fig. S1a. The composition of the catalyst changed from $Pt_{51}Ni_{49}$ to $Pt_{55}Ni_{45}$. AFM Images in Fig. S1b show that the morphology of the sample remained intact.

Fig. 1b summarizes cyclic voltammogram (CV) curves acquired in N_2-saturated 0.1 M KOH electrolyte for the as-deposited PtNi (green curve), the PtNi after treatment in 0.1 M H_2SO_4, denoted as Pt-skin (blue curve), and the reference monometallic Pt denoted as Pt_{ref} (red curve). The as-deposited PtNi did not reveal any sharp features characteristic of platinum, which is attributed to the presence of an oxide/hydroxide layer on the sample surface formed by its transfer from the deposition

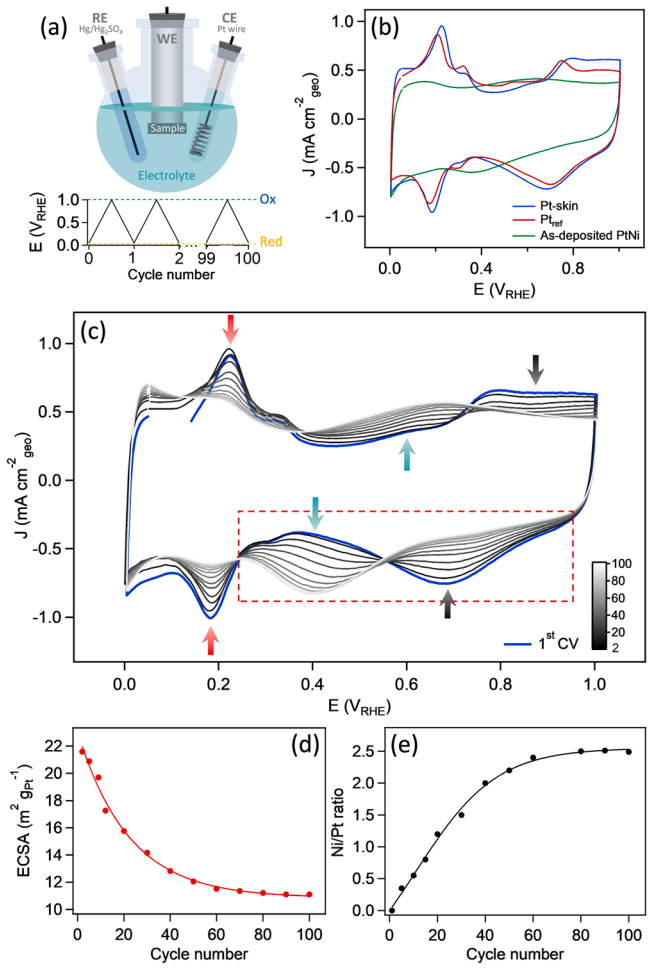

Fig. 1. (a) Schematic illustration of cyclic voltammetry setup together with the applied cycling protocol; (b) Cyclic voltammograms of as-deposited PtNi (green), PtNi after 30 s in 0.5 M H_2SO_4, denoted as Pt-skin (blue), and monometallic Pt (red) recorded in N_2-saturated 0.1 M KOH at 200 $mV{\cdot}s^{-1}$ sweep rate; (c) The series of 100 cyclic voltammograms recorded on Pt-skin sample (arrows indicate changes in the CVs shape during cycling: red arrows highlights H_{UPD} decrease, green arrows highlights an increase in adsorption/desorption of OH^- on Ni atoms placed on the Pt surface and black arrows highlights a decrease in Pt oxidation/reduction couple); (d) Evolution of electrochemically active surface area (ECSA) calculated from cyclic voltammograms shown in (c); (e) Ni/Pt ratio calculated from deconvoluted Pt and Ni reduction peaks highlighted by the rectangle in (c).

chamber to the electrochemical cell through the air. Note, that the acid-treated sample (Pt-skin) was transferred to the electrochemical cell without sample exposure to the air to avoid its re-oxidation. After acid treatment, the CV curve appears virtually identical to that for pure Pt featuring typical fingerprints of polycrystalline Pt electrodes in an alkaline electrolyte i.e., an underpotentially deposited hydrogen (H_{UPD}) region within 0–0.40 V_{RHE} followed by adsorption/desorption of oxygenated species on the Pt surface. This unambiguously demonstrates a vanishing of all Ni and Ni-oxides from the surface by acid treatment and formation of the so-called Pt-skin surface [39].

The Pt-skin sample was then subjected to 100 CV cycles from 0 to 1.0 V_{RHE}. The evolution of corresponding voltammograms is depicted in Fig. 1c. One can qualitatively observe three interconnected phenomena co-occurring during the cycling: (i) emerging and progressive increase of the redox couple around 0.6 and 0.4 V_{RHE} in anodic and cathodic scans, respectively, (highlighted by green arrows) that could be attributed to the adsorption/desorption of OH^- on Ni atoms placed on the Pt surface [40–42]; (ii) a gradual decreasing of the peaks corresponding to oxidation and reduction of Pt within the range 0.6–1.0 V_{RHE} (highlighted by grey arrows); (iii) continuous regression of the H_{UPD} charge within the range 0–0.4 V_{RHE} (highlighted by red arrows). All these factors evidence the gradual accumulation of Ni atoms on the surface of the alloy after each redox cycle. Similar results were reported previously by Mayrhofer et al. during overnight potential cycling of pre-leached Pt_3Co nanoparticles [38].

To estimate the decrease in Pt active centers on the surface of the Pt-skin catalyst during repetitive CV cycling, the electrochemically active surface area (ECSA) was determined by integrating the hydrogen desorption peaks from corresponding CV curves. The results shown in Fig. 1d demonstrate about a 50% decrease in ECSA from its value for the second cycle during the entire cycling procedure. Note that we could not calculate ECSA for the first cycle, i.e. Pt-skin, because CV is interrupted at the hydrogen desorption region. As a result, we expect a slightly greater reduction of ECSA during electrochemical cycling. We also excluded a possible influence of catalyst coarsening on ECSA since the morphology of the sample after 100 CV cycles measured *ex situ* by AFM did not differ substantially from that acquired for the Pt-skin sample (See Fig. S1b).

In order to quantify the observed surface restructuring, we disentangled the peaks corresponding to Ni and Pt reduction on the cathodic sweep of CVs (highlighted in Fig. 1c by the red rectangle). The detailed explanation of the deconvolution process can be found in ESI. Based on deconvolution, the relative Ni/Pt ratio was calculated as Ni_{red} charge divided by Pt_{red} charge, and its evolution during the entire cycling procedure is depicted in Fig. 1e. The results indicate Ni segregation onto the catalyst surface with increasing cycle number. The Ni/Pt ratio increased rapidly at the beginning of cycling and saturated at a value of about 2.5 after 60 CV cycles corresponding to $Pt_{28}Ni_{72}$, which is in agreement with the ECSA behaviour in Fig. 1d. *Ex situ* EDX acquired before and after cycling in Fig. S1a shows an identical bulk composition, which points to the fact that the compositional changes occur close to the surface of the bimetallic alloy only.

A further question arises of how the above-described catalyst surface modifications affect reactivity. We demonstrated this by evaluating catalyst activity towards the methanol electrooxidation reaction (MOR) in an alkaline electrolyte.

Fig. 2a displays CVs acquired in 0.1 M KOH + 0.5 M CH_3OH solution for Pt-skin, Pt-skin after 100 CV in KOH, and the Pt_{ref} catalysts. Fig. 2b, in turn, shows corresponding CVs recorded in N_2-saturated 0.1 M KOH without methanol for a better comparison. Note that MOR after 100 CV in KOH was tested without exposing the sample to air. The forward scan in Fig. 2a exhibited the intense oxidation peak (J_f) at about 0.7 V_{RHE} (see Table 1) related to initial methanol electrooxidation, while another less intense oxidation peak (J_b) appeared at about 0.6 V_{RHE} (see Table 1) in the backward scan attributed to the oxidation of carbon-containing intermediate products (mostly CO_{ads}) formed during the forward scan. Similar to CV without methanol (Fig. 2b), Pt-skin exhibited slightly higher currents than the Pt_{ref}, implying a higher activity towards MOR. It should also be kept in mind that the PtNi samples contain a twice lower amount of Pt, pointing to an even higher mass activity of the Pt-skin catalyst. More importantly, Pt-skin showed a much higher J_f/J_b ratio (2.91) than the reference Pt (1.75), indicating its better ability to resist poisoning than monometallic Pt. This agrees well with earlier studies on the MOR activity of Pt and PtNi alloys [43–48].

After a series of oxidation/reduction cycles, significant Ni enrichment at the surface of the Pt-skin sample described above resulted in a considerable decrease in electrocatalytic activity toward MOR, as shown in Fig. 2a and Table 1. This is apparently attributed to the blocking of Pt active sites caused by Ni accumulation on the surface. Indeed, the charge of the methanol oxidation peak in the forward scan dropped by about 60%, which is in close agreement with a decrease of ECSA and an increase of Ni/Pt ratio determined during cycling in 0.1 M KOH solution (see Fig. 1d and e).

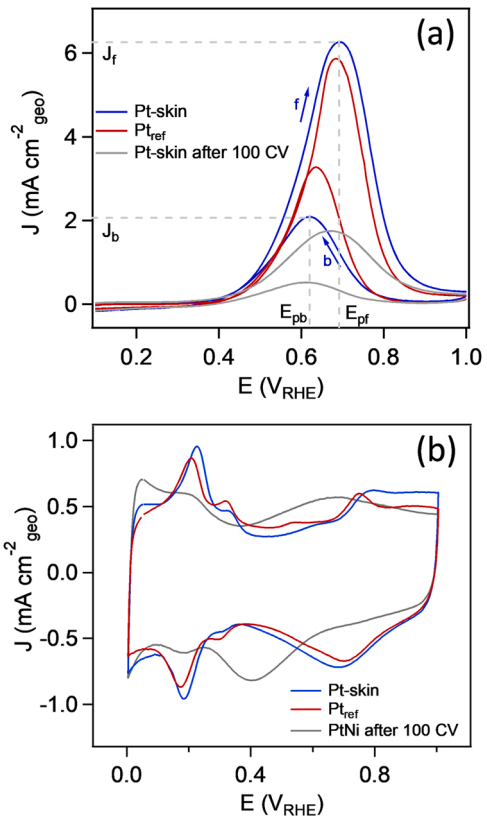

Fig. 2. (a) Cyclic voltammograms for the electrooxidation of methanol over Pt-skin (blue), Pt-skin after 100 CV in N_2-saturated 0.1 M KOH (grey) and reference Pt (red) recorded in N_2-saturated 0.1 M KOH + 0.5 M CH_3OH solution at 50 mV·s^{-1} sweep rate (Arrows indicate forward and backward sweeps. J_f and J_b indicate maximum current density in forward and backward sweeps, respectively. E_{pf} and E_{pb} indicate the position of peaks in forward and backward sweeps, respectively); (b) Cyclic voltammograms of Pt-skin (blue), Pt-skin after 100 CV (grey) and reference Pt (red) recorded in N_2-saturated 0.1 M KOH at 200 mV·s^{-1} sweep rate.

Table 1
Catalytic performance of Pt-based electrocatalysts for methanol electrooxidation in 0.1 M KOH + 0.5 M CH_3OH solution at 50 mV s^{-1} sweep rate: E_{pf} – position of the peak in forward direction, E_{pb} – position of the peak in backward direction, J_f – maximum current density of the peak in forward direction, J_b – maximum current density of the peak in backward direction.

Sample	E_{pf} (V_{RHE})	E_{pb} (V_{RHE})	J_f (mA·cm^{-2})	J_b (mA·cm^{-2})	J_f/J_b
Pt_{ref}	0.68	0.63	5.755	3.280	1.75
Pt-skin	0.69	0.62	6.082	2.092	2.91
Pt-skin (100 CV)	0.67	0.61	1.593	0.539	2.96

3.2. Near-ambient pressure XPS study

NAP-XPS was then employed to gain more insights into the chemistry occurring on the surface of the PtNi catalyst during its successive oxidation and reduction. For that, a set of alternating oxidizing (5 mbar of O_2) and reducing (5 mbar of H_2) environments at 100 °C and 250 °C were established in the NAP chamber as schematically illustrated in Fig. 3a.

Before the redox experiment itself, the as-deposited PtNi catalyst was treated first with a reducing hydrogen atmosphere (5 mbar of H_2) for 1 h and then with a mild Ar bombardment in UHV to remove surface contaminants, including Ni oxides/hydroxides and further annealed in UHV to 250 °C. As was shown in our previous study using DFT calculations, under these conditions, the lowest-energy homotops of PtNi nanoparticle exhibited a structure with the outer shell formed mostly of Pt atoms, which should be comparable with the Pt-skin structure used for the CV experiment, as illustrated in Fig. 3c [31]. The characteristic spectra of the PtNi sample recorded before and after the cleaning procedure are presented in Fig. S3. The Pt 4f and Ni $2p_{3/2}$ spectra, after cleaning, contained metallic characteristics only. Furthermore, oxygen contribution completely vanished, as highlighted by the O 1s spectral line. A more detailed description of the spectra can be found in the Electronic Supporting Information (ESI). The elemental composition of the cleaned catalyst, estimated from the fitted Pt 4f and Ni 3p spectra, was $Pt_{48}Ni_{52}$. The alloy formation in such magnetron co-sputtered PtNi layers has been confirmed repeatedly in our previous studies [14,34,49].

Pt 4f and Ni 3p core levels were of primary interest in providing information about the surface composition. They appear close to each other on the photoelectron spectrum, i.e., acquired at an identical photon flux, transmission function, and surface information depth. In this case, the identical probing depth for both Pt and Ni was reached. Since Pt 4f and Ni 3p spectra are partially overlapping, the Ni 3p XPS spectra of a reference monometallic nickel and nickel oxide were measured prior to the experiment (see Fig. S5) and results were used for the reliable fitting of the resulting Pt 4f + Ni 3p spectra of the PtNi alloy [50]. A detailed description of the Ni 3p XPS spectra recorded for the reference monometallic nickel and pure nickel oxide are shown in ESI. XPS Pt 4f + Ni 3p spectra after cleaning were then compared in Fig. S4 with that for Pt-skin sample in the cyclic voltammetry experiment. The corresponding spectra were practically identical with only negligible deviations in sample composition ($Pt_{48}Ni_{52}$ vs. $Pt_{50}Ni_{50}$), indicating a similar starting point for both experiments.

Once clean and characterized, the alloy catalyst was transferred from the UHV chamber to the NAP cell and subjected to repetitive oxidizing and reducing atmospheres. We commenced with a discussion of redox cycling at 250 °C as PtNi showed more pronounced changes under these conditions, which are more clearly visible by NAP-XPS. The corresponding Pt 4f and Ni 3p core levels were acquired directly in the corresponding gaseous environment. Fig. 3b represents high-resolution NAP-XPS spectra recorded during the first oxidation (middle spectrum, denoted as Ox1) and the following first reduction (upper spectrum, denoted as Red1) steps. To facilitate the comparison, both spectra were compared with the one recorded before exposure to reactive atmospheres (bottom spectrum, denoted as cleaned).

During oxidation, platinum remained in the metallic state with a clear doublet at 71.15–74.5 eV [21,51]. It was, however, slightly shifted to lower binding energies as compared to the sample before oxidation (71.3–74.6 eV), suggesting some structural changes. Meanwhile, Ni was clearly oxidized to NiO, showing the doublet at 66.8–68.7 eV and the corresponding satellite features at 71.3–73.5 eV [52–54]. The O 1 s spectral line shown in Fig. S6a can be deconvoluted into several components, including the gas phase contribution within 536–542 eV and two well-resolved peaks at 529.4 and 531.3 eV. The former associates with oxygen from NiO, and the latter is assigned to defective sites within the NiO structure [24,55]. The above observations correlate well with the analysis of the Ni $2p_{3/2}$ spectrum, which is shown in Fig. S6b (middle spectrum) where the typical NiO multiplet splitting can be observed. Furthermore, the abovementioned nickel oxidation attenuates the Pt 4f signal pointing to the outward diffusion of Ni and the formation of Ni-oxide on the surface of the alloy. The elemental composition, calculated from the NAP-XPS spectrum (middle spectrum in Fig. 3b), is $Pt_{15}Ni_{85}$. This composition could correspond to a fully oxidized NiO shell on the catalyst surface, as predicted by Liu et al. [56], but according to the previous *operando* microscopy studies on high-temperature oxidation of PtNi alloys, the NiO rather grows as homogeneously distributed three-dimensional NiO islands, as schematically illustrated in Fig. 3c [24,57].

It is also important to emphasize that the oxidation of PtNi was apparently limited to Ni atoms only, while Pt remained in the metallic

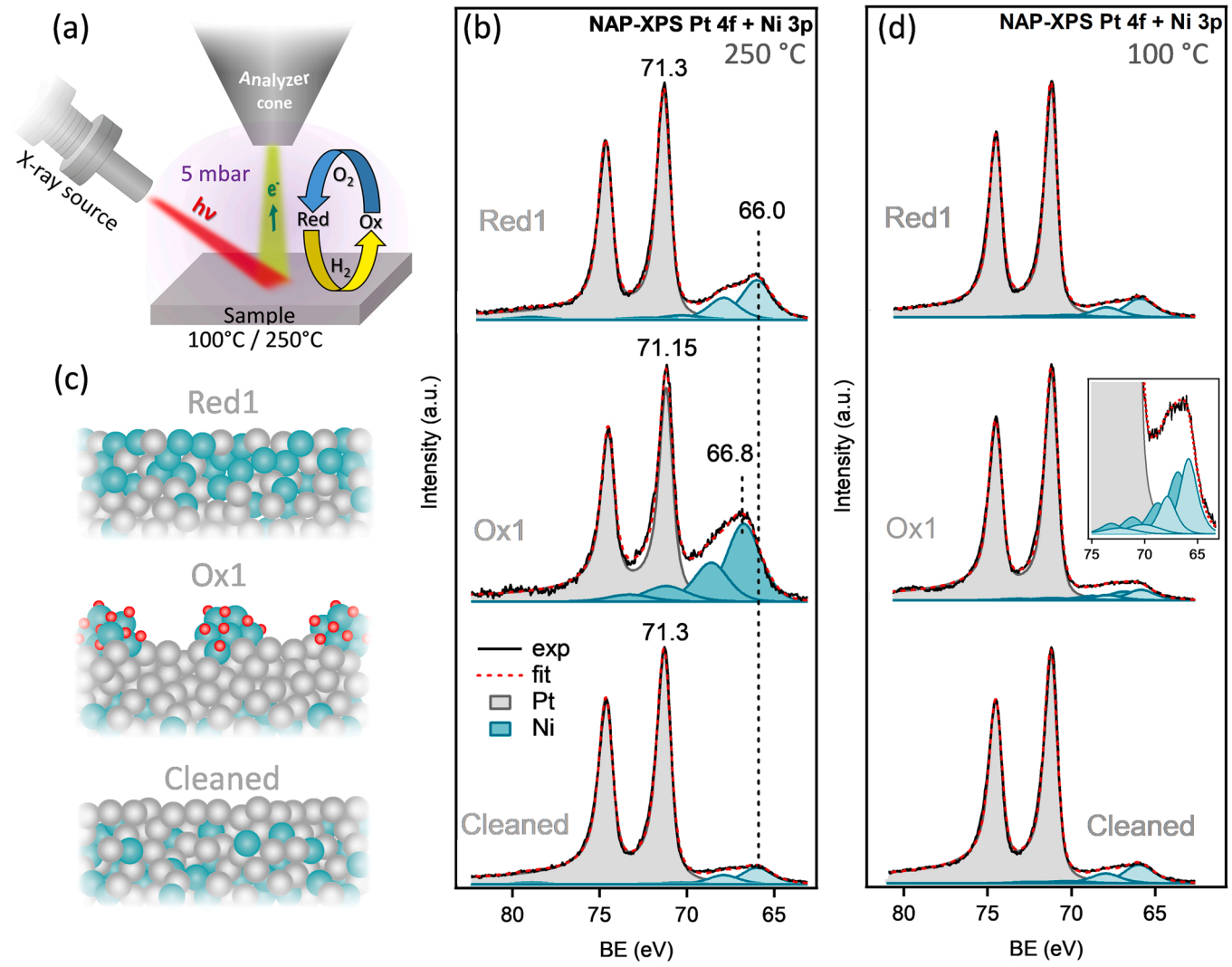

Fig. 3. (a) Schematic illustration of NAP-XPS setup. The sample was characterized *in situ* under alternating 5 mbar oxygen and 5 mbar hydrogen atmospheres at 100 °C and 250 °C; (b) Pt 4f + Ni 3p NAP-XPS spectra of PtNi alloy acquired before (denoted as cleaned), under first oxidation (5 mbar O_2, denoted as Ox1) and subsequent first reduction (5 mbar H_2, denoted as Red1) steps at 250 °C; (c) Schematic illustration of compositional changes on the surface of PtNi alloy in response to alternating oxidizing and reducing environments (d) Pt 4f + Ni 3p spectra of PtNi alloy acquired before (denoted as cleaned), under first oxidation (5 mbar O_2, denoted as Ox1) and subsequent first reduction (5 mbar H_2, denoted as Red1) at 100 °C. Inset highlights the Ni 3p region for the sample under first oxidation.

state. This led to dealloying of the catalyst surface in the presence of oxygen and could explain the slight shift (0.15 eV) of the Pt 4f component to lower binding energies discussed above. Similar phase separations were previously observed in the case of the model Pt/Ni(111) system using NAP-XPS and explained by an almost six-fold higher affinity of Ni for oxygen as compared to Pt [24]. On the other hand, in our previous study, a small amount of Pt^{2+} was observed during PtNi oxidation, which was attributed to surface mixed oxides [31]. This inconsistency might be explained by the fact that we used synchrotron radiation of low photon energy with the probing depth set up to three monolayers. Apparently, this small amount of Pt^{2+} could not be detected by standard laboratory XPS used in this study with about 5 nm probing depth.

As the gas switched from oxidizing to reducing (Red1), the surface recovered to metallic Pt and Ni elements as shown in Fig. 3b (upper spectrum), which is also supported by the absence of the oxygen contribution in the O 1s spectrum shown at the top of Fig. S6a. A single set of Ni peaks, i.e. a doublet at 66.0–67.8 eV and satellites at 70.3–72.4 eV, appears in the Ni 3p spectrum representing a metallic phase [31,58]. The Pt 4f spectrum shifted back to 71.3–74.6 eV, demonstrating realloying [59,60]. The calculated elemental composition of PtNi alloy after reduction was $Pt_{30}Ni_{70}$. Notably, the surface composition did not entirely recover to its initial value of $Pt_{48}Ni_{52}$ before the Ox1 step, demonstrating a significant increase in the amount of nickel, thereby leaving some compositional non-uniformity within the PtNi layer, as schematically illustrated in Fig. 3c. Surprisingly, these results are almost identical to those in our previous study, where an identical experiment was performed *ex situ* in a separate chamber [31]. This indicates the strong stability of redox-driven surface compositional change. We explained the surface composition irreversibility under alternating oxidation/reduction conditions by DFT calculations using 4.4 nm large truncated octahedral 1463-atomic NP with $Pt_{731}Ni_{732}$ stoichiometry. It was shown that hydrogen adsorption was not energetically sufficient to reverse fully the Pt covered by Ni atoms because the adsorption energy for hydrogen is an order of magnitude lower than that for oxygen.

When the temperature was lower i.e. 100 °C, the overall behavior of the PtNi catalyst was identical to that described for 250 °C. However, the observed changes were much less pronounced. The only difference is that under oxidizing environment (Ox1) at 100 °C, nickel was not fully oxidized. As can be seen in the middle spectrum in Fig. 3d, the Ni 3p region is composed of mixed metallic and oxide states. These

observations are supported by the analysis of the Ni $2p_{3/2}$ spectrum, shown in Fig. S6c. This could be attributed to the fact that at 100 °C, oxidation and thus Ni segregation is limited to a few upper atomic layers of the PtNi alloy only, while a significant amount of Ni atoms deeper in the alloy are not influenced by the reactive atmosphere and remain in metallic state.

The main output of the NAP-XPS experiment is summarized in Fig. 4. The set of Pt 4f + Ni 3p NAP-XPS spectra recorded under five sequential oxidizing/reducing environments at 250 °C and 100 °C are shown in Figs. 4a and 4c, respectively. For comparison, the simultaneously captured Ni $2p_{3/2}$ spectra are shown in Fig. S7. In turn, the relative Ni/Pt atomic ratio, quantified from Ni 3p and Pt 4f peaks area taking into account the corresponding photoionization cross-sections, is plotted for all five oxidation and reduction steps at 250 °C and 100 °C in Figs. 4b and 4d, respectively.

The results show an oscillatory behaviour for both temperatures with Ni oxidation and enrichment under the oxidizing environment and its subsequent reduction and reincorporation into the PtNi alloy under the reducing environment. However, a closer inspection of the Ni/Pt ratio at reduction steps points to the irreversible change of PtNi surface composition with redox cycle number. The Ni/Pt ratio increased at the beginning of cycling and was saturated after the third-fourth redox cycle. Overall, during the entire cycling procedure at 250 °C, the surface composition of the PtNi changed significantly from $Pt_{48}Ni_{52}$ to $Pt_{20}Ni_{80}$ (Ni/Pt ratio 3.9) while at 100 °C it changed to only $Pt_{43}Ni_{57}$ (Ni/Pt ratio 1.3). Following rapid initial compositional changes in favor of nickel, the bimetallic catalyst apparently reaches a metastable composition that is kinetically hindered from further changes. Based on the fact that the composition of the sample measured before and after redox cycling with a bulk-sensitive EDX technique showed no substantial changes (see Fig. S8), we can conclude that the above compositional changes occur on the surface of the bimetallic alloy only.

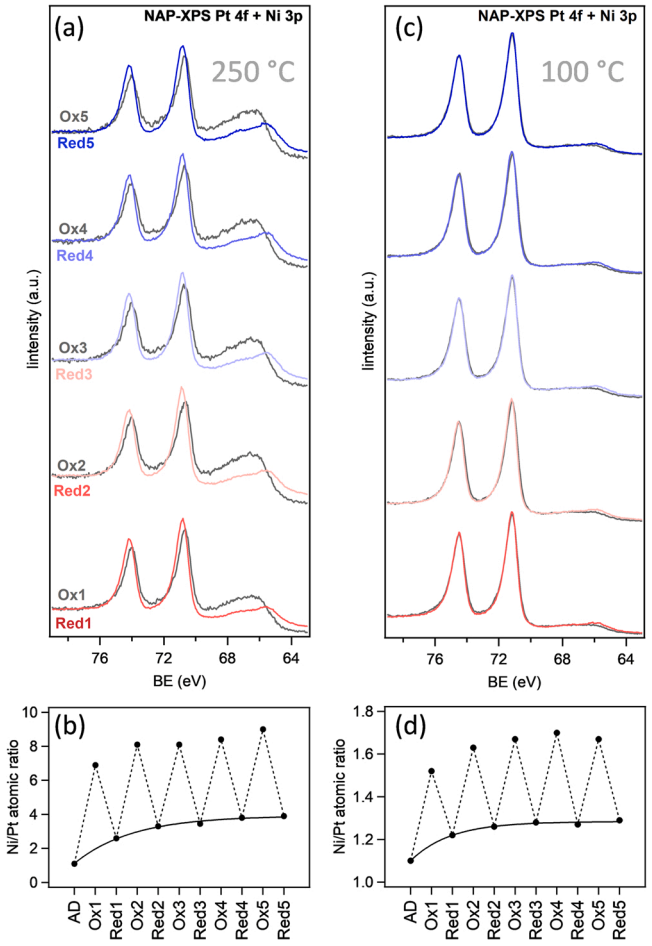

Fig. 4. Pt 4f + Ni 3p NAP-XPS spectra of PtNi alloy acquired under five oxidations (5 mbar O_2) and five subsequent reductions (5 mbar H_2) at (a) 250 °C and (c) 100 °C; Evolution of Ni/Pt atomic ratio during five oxidation/reduction cycles at (b) 250 °C and (d) 100 °C, extracted from the integrated areas of the Pt 4f and Ni 3p NAP-XPS spectra divided by the corresponding photoionization cross-sections.

This behavior also correlates with the results obtained during the electrochemical oxidation and reduction of the PtNi alloy. Even though the results appeared to be qualitatively identical, it is impossible to quantitatively compare compositional changes based on these experiments due to significantly different probing depths of CV (outermost layer only) and NAP-XPS techniques (~5 nm). In order to juxtapose the results obtained under different environments, we compared the XPS spectra captured after five redox cycles in a gaseous atmosphere with the *ex situ* XPS spectra acquired after electrochemical cycling. The spectra are shown in Fig. S9 and relative atomic compositions calculated from corresponding spectra are summarised in Table 2 together with those measured before redox cycling. The results show comparable changes in PtNi composition during CV cycling to that acquired during redox cycling in gaseous environments at 100 °C. These observations suggest that similar processes occur during redox cycling in the electrified liquid environment, as well as in gaseous atmospheres at 100 °C. Taking into account significant compositional changes observed from the CVs and significantly lower changes measured by NAP-XPS, we can conclude that redistribution occurs only within the few (2−3) top atomic layers of the PtNi alloy. However, the depth where compositional changes occur, strongly depended on the temperature. Redox cycling in gaseous environments at 250 °C led to significantly greater compositional changes, apparently associated with the enhanced atoms mobility caused by the elevated temperature. Indeed, surface segregation depends on the diffusion and mobility of metal atoms and elevated temperature provides the activation energy, which allows the transfer of metal atoms from the deeper layer of the alloy [21,29,30].

The presented results reveal complex dynamic processes occurring on the surface of bimetallic catalyst systems in response to a reactive environment. Understanding and controlling these processes is therefore of great importance towards the preparation of active and stable catalysts for many reactions by its interfacial engineering.

4. Conclusions

Using *in situ* electrochemical and spectroscopic studies, we demonstrated a surface restructuring of a PtNi alloy catalyst under repetitive oxidation and reduction conditions, simulating inherent working conditions for numerous catalytic redox reactions.

Under potential-driven oxidation and reduction at electrified solid/liquid interface utilizing cyclic voltammetry, the PtNi alloy composition was found to be unstable. Under a series of potentiodynamic oxidation/reduction cycles, the composition of the outermost layer, calculated from the recorded cyclic voltammograms, changed from Pt-skin with no Ni on the surface ($Pt_{100}Ni_0$) to the Ni-enriched one ($Pt_{28}Ni_{72}$). However, the less surface-sensitive *ex situ* XPS showed much smaller changes in sample composition indicating that redistribution occurs solely within the few (2−3) top atomic layers of the PtNi alloy.

We demonstrated how changes in the surface composition profile

Table 2
Relative atomic compositions of PtNi alloy calculated from Pt 4f and Ni 3p XPS spectra acquired before and after redox cycling at electrified liquid environment and gaseous environment at 100 °C and 250 °C.

	NAP-XPS (250 °C)	NAP-XPS (100 °C)	XPS (CV)
Before	$Pt_{48}Ni_{52}$	$Pt_{48}Ni_{52}$	$Pt_{50}Ni_{50}$
After	$Pt_{20}Ni_{80}$	$Pt_{43}Ni_{57}$	$Pt_{45}Ni_{55}$

caused by redox cycling affected the PtNi reactivity using methanol electrooxidation as a model reaction. A 60% decrease in activity towards methanol electrooxidation was measured, confirming catalyst deactivation as a result of irreversible compositional changes.

The near-ambient pressure X-ray photoelectron spectroscopy was used to gain more insights into the chemistry occurring on the surface of the PtNi catalyst during its alternating cycles of oxidation and reduction. It was revealed that alternating oxidation (5 mbar of O_2) and reduction (5 mbar of H_2) atmospheres at 100 °C and 250 °C caused catalyst oxidation and reduction at each cycle. The oxidation and reduction of PtNi were, however, limited to Ni atoms only, while Pt remained in the metallic state regardless of the reactive atmosphere. This led to catalyst surface dealloying/realloying during each redox cycle. In the course of five such dealloying/realloying cycles, PtNi underwent irreversible changes on the surface, which strongly affected its compositional profile in terms of surface nickel enrichment. The observed change, however, was much higher at 250 °C than at 100 °C. The quantified PtNi surface composition changed with redox cycle number from $Pt_{48}Ni_{52}$ to $Pt_{20}Ni_{80}$ at 250 °C and to $Pt_{43}Ni_{57}$ at 100 °C. The latter is comparable to that measured by XPS before and after electrochemical cycling.

CRediT authorship contribution statement

Xianxian Xie: Investigation, Formal analysis, Data curation, Writing – review & editing. **Athira Lekshmi Mohandas Sandhya:** Investigation, Formal analysis, Writing – review & editing. **Lesia Piliai:** Investigation, Formal analysis, Writing – review & editing. **Mykhailo Vorokhta:** Investigation, Formal analysis, Data curation, Writing – review & editing. **Iva Matolínová**: Data curation, Supervision, Writing – review & editing. **Ivan Khalakhan**: Conceptualization, Data curation, Writing – original draft, Writing – review & editing, Supervision, Funding acquisition.

Declaration of Competing Interest

The authors declare that they have no known competing financial interests or personal relationships that could have appeared to influence the work reported in this paper.

Data Availability

Data will be made available on request.

Acknowledgments

The work was financially supported by the Czech Science Foundation, project No. 22–03643S. The authors further acknowledge the CERIC-ERIC consortium for access to the experimental facility and financial support.

Appendix A. Supporting information

Supplementary data associated with this article can be found in the online version at doi:10.1016/j.apcatb.2022.122328.

References

[1] K.D. Gilroy, A. Ruditskiy, H.-C. Peng, D. Qin, Y. Xia, Bimetallic nanocrystals: syntheses, properties, and applications, Chem. Rev. 116 (2016) 10414–10472.
[2] J. Greeley, I.E.L. Stephens, A.S. Bondarenko, T.P. Johansson, H.A. Hansen, T. F. Jaramillo, J. Rossmeisl, I. Chorkendorff, J.K. Nørskov, Alloys of platinum and early transition metals as oxygen reduction electrocatalysts, Nat. Chem. 1 (2009) 552–556.
[3] V. Stamenkovic, B.S. Mun, K.J.J. Mayrhofer, P.N. Ross, N.M. Markovic, J. Rossmeisl, J. Greeley, J.K. Nørskov, Changing the activity of electrocatalysts for oxygen reduction by tuning the surface electronic structure, Angew. Chem. Int. Ed. 45 (2006) 2897–2901.
[4] J. Greeley, J.K. Nørskov, L.A. Kibler, A.M. El-Aziz, D.M. Kolb, Hydrogen evolution over bimetallic systems: understanding the trends, ChemPhysChem 7 (2006) 1032–1035.
[5] G.A. Tritsaris, J. Rossmeisl, Methanol oxidation on model elemental and bimetallic transition metal, Surf., J. Phys. Chem. C. 116 (2012) 11980–11986.
[6] C. Te Hsieh, J.Y. Lin, Fabrication of bimetallic Pt-M (M = Fe, Co, and Ni) nanoparticle/carbon nanotube electrocatalysts for direct methanol fuel cells, J. Power Sources 188 (2009) 347–352.
[7] Y. Wang, S. Zou, W.-B. Cai, Recent advances on electro-oxidation of ethanol on Pt- and Pd-based catalysts: from reaction mechanisms to catalytic materials, Catalysts 5 (2015) 1507–1534.
[8] T. Bligaard, J.K. Nørskov, Ligand effects in heterogeneous catalysis and electrochemistry, Electrochim. Acta 52 (2007) 5512–5516.
[9] S. Shan, V. Petkov, B. Prasai, J. Wu, P. Joseph, Z. Skeete, E. Kim, D. Mott, O. Malis, J. Luo, C.J. Zhong, Catalytic activity of bimetallic catalysts highly sensitive to the atomic composition and phase structure at the nanoscale, Nanoscale 7 (2015) 18936–18948.
[10] C. Wei, Y. Sun, G.G. Scherer, A.C. Fisher, M. Sherburne, J.W. Ager, Z.J. Xu, Surface composition dependent ligand effect in tuning the activity of nickel–copper bimetallic electrocatalysts toward hydrogen evolution in alkaline, J. Am. Chem. Soc. 142 (2020) 7765–7775.
[11] F. Tao, M.E. Grass, Y. Zhang, D.R. Butcher, J.R. Renzas, Z. Liu, J.Y. Chung, B. S. Mun, M. Salmeron, G.A. Somorjai, Reaction-driven restructuring of Rh-Pd and Pt-Pd core-shell nanoparticles, Science 322 (2008) 932–934.
[12] S. Zafeiratos, S. Piccinin, D. Teschner, Alloys in catalysis: phase separation and surface segregation phenomena in response to the reactive environment, Catal. Sci. Technol. 2 (2012) 1787–1801.
[13] F. Tao, S. Zhang, N. Luan, X. Zhang, Action of bimetallic nanocatalysts under reaction conditions and during catalysis: evolution of chemistry from high vacuum conditions to reaction conditions, Chem. Soc. Rev. 41 (2012) 7980–7993.
[14] I. Khalakhan, M. Bogar, M. Vorokhta, P. Kúš, Y. Yakovlev, M. Dopita, D.J. S. Sandbeck, S. Cherevko, I. Matolínová, H. Amenitsch, Evolution of the PtNi bimetallic alloy fuel cell catalyst under simulated operational conditions, ACS Appl. Mater. Interfaces 12 (2020) 17602–17610.
[15] Y.-T. Pan, H. Yang, Design of bimetallic catalysts and electrocatalysts through the control of reactive environments, Nano Today 31 (2020), 100832.
[16] Y. Zhu, J. Wang, H. Chu, Y.-C. Chu, H.M. Chen, In situ/operando studies for designing next-generation electrocatalysts, ACS Energy Lett. 5 (2020) 1281–1291.
[17] A. Bergmann, B. Roldan, Cuenya, operando insights into nanoparticle transformations during catalysis, ACS Catal. 9 (2019) 10020–10043.
[18] H.L. Xin, S. Alayoglu, R. Tao, A. Genc, C.M. Wang, L. Kovarik, E.A. Stach, L. W. Wang, M. Salmeron, G.A. Somorjai, H. Zheng, Revealing the atomic restructuring of Pt-Co nanoparticles, Nano Lett. 14 (2014) 3203–3207.
[19] S. Dai, Y. You, S. Zhang, W. Cai, M. Xu, L. Xie, R. Wu, G.W. Graham, X. Pan, In situ atomic-scale observation of oxygen-driven core-shell formation in Pt3Co nanoparticles, Nat. Commun. 8 (2017) 204.
[20] K.J.J. Mayrhofer, V. Juhart, K. Hartl, M. Hanzlik, M. Arenz, Adsorbate-Induced surface segregation for core-shell nanocatalysts, Angew. Chem. - Int. Ed. 48 (2009) 3529–3531.
[21] M. Ahmadi, F. Behafarid, C. Cui, P. Strasser, B.R. Cuenya, Long-range segregation phenomena in shape-selected bimetallic nanoparticles: chemical state effects, ACS Nano 7 (2013) 9195–9204.
[22] T.-S. Kim, J. Kim, H.C. Song, D. Kim, B. Jeong, J. Lee, J.W. Shin, R. Ryoo, J.Y. Park, Catalytic synergy on PtNi bimetal catalysts driven by interfacial intermediate structures, ACS Catal. 10 (2020) 10459–10467.
[23] C. Cui, L. Gan, M. Heggen, S. Rudi, P. Strasser, Compositional segregation in shaped Pt alloy nanoparticles and their structural behaviour during electrocatalysis, Nat. Mater. 12 (2013) 765–771.
[24] J. Kim, W.H. Park, W.H. Doh, S.W. Lee, M.C. Noh, J.-J. Gallet, F. Bournel, H. Kondoh, K. Mase, Y. Jung, B.S. Mun, J.Y. Park, Adsorbate-driven reactive interfacial Pt-NiO1−x nanostructure formation on the $Pt_3Ni(111)$ alloy surface, Sci. Adv. 4 (2018) eaat3151.
[25] S. Chen, Z. Niu, C. Xie, M. Gao, M. Lai, M. Li, P. Yang, Effects of catalyst processing on the activity and stability of Pt–Ni nanoframe electrocatalysts, ACS Nano 12 (2018) 8697–8705.
[26] K.J. Andersson, F. Calle-Vallejo, J. Rossmeisl, I. Chorkendorff, Adsorption-driven surface segregation of the less reactive alloy component, J. Am. Chem. Soc. 131 (2009) 2404–2407.
[27] J. Wang, X. Chang, S. Chen, G. Sun, X. Zhou, E. Vovk, Y. Yang, W. Deng, Z.-J. Zhao, R. Mu, C. Pei, J. Gong, On the role of Sn segregation of Pt-Sn catalysts for propane dehydrogenation, ACS Catal. 11 (2021) 4401–4410.
[28] Y. Uemura, Y. Inada, K.K. Bando, T. Sasaki, N. Kamiuchi, K. Eguchi, A. Yagishita, M. Nomura, M. Tada, Y. Iwasawa, Core−shell phase separation and structural transformation of Pt_3Sn alloy nanoparticles supported on γ-Al_2O_3 in the reduction and oxidation processes characterized by in situ time-resolved XAFS, J. Phys. Chem. C. 115 (2011) 5823–5833.
[29] H. Liao, A. Fisher, Z.J. Xu, Surface segregation in bimetallic nanoparticles: a critical issue in electrocatalyst engineering, Small 11 (2015) 3221–3246.
[30] N. Zhang, Q. Shao, X. Xiao, X. Huang, Advanced catalysts derived from composition-segregated platinum–nickel nanostructures: new opportunities and challenges, Adv. Funct. Mater. 29 (2019) 1808161.
[31] I. Khalakhan, L. Vega, M. Vorokhta, T. Skála, F. Viñes, Y.V. Yakovlev, K. M. Neyman, I. Matolínová, Irreversible structural dynamics on the surface of bimetallic PtNi alloy catalyst under alternating oxidizing and reducing environments, Appl. Catal. B Environ. 264 (2020), 118476.

[32] J. Suntivich, Z. Xu, C.E. Carlton, J. Kim, B. Han, S.W. Lee, N. Bonnet, N. Marzari, L. F. Allard, H.A. Gasteiger, K. Hamad-Schifferli, Y. Shao-Horn, Surface composition tuning of Au–Pt bimetallic nanoparticles for enhanced carbon monoxide and methanol electro-oxidation, J. Am. Chem. Soc. 135 (2013) 7985–7991.
[33] P.P. Lopes, D. Li, H. Lv, C. Wang, D. Tripkovic, Y. Zhu, R. Schimmenti, H. Daimon, Y. Kang, J. Snyder, N. Becknell, K.L. More, D. Strmcnik, N.M. Markovic, M. Mavrikakis, V.R. Stamenkovic, Eliminating dissolution of platinum-based electrocatalysts at the atomic scale, Nat. Mater. 19 (2020) 1207–1214.
[34] I. Khalakhan, L. Supik, M. Vorokhta, Y. Yakovlev, M. Dopita, D.J.S. Sandbeck, S. Cherevko, K. Veltruská, I. Matolínová, Compositionally tuned magnetron co-sputtered Pt_xNi_{100-x} alloy as a cathode catalyst for proton exchange membrane fuel cells, Appl. Surf. Sci. 511 (2020), 145486.
[35] J. Libra, KolXPD: Software for spectroscopy data measurement and processing, http://www.kolibrik.net/science/kolxpd/, Kolibrik.net, s.r.o., Žďár nad Sázavou, Czech Republic, (n.d.).
[36] J.F. Rusling, S.L. Suib, Characterizing materials with cyclic voltammetry, Adv. Mater. 6 (1994) 922–930.
[37] M. Pourbaix, Atlas of electrochemical equilibria in aqueous solutions, (2nd English Ed.), Natl. Assoc. Corros. Eng. (1974) 551 pages.
[38] K.J.J. Mayrhofer, K. Hartl, V. Juhart, M. Arenz, Degradation of carbon-supported Pt bimetallic nanoparticles by surface segregation, J. Am. Chem. Soc. 131 (2009) 16348–16349.
[39] V.R. Stamenkovic, B.S. Mun, K.J.J. Mayrhofer, P.N. Ross, N.M. Markovic, Effect of surface composition on electronic structure, stability, and electrocatalytic properties of Pt-transition metal alloys: Pt-skin versus Pt-skeleton surfaces, J. Am. Chem. Soc. 128 (2006) 8813–8819.
[40] R. Subbaraman, D. Tripkovic, D. Strmcnik, K.-C. Chang, M. Uchimura, A. P. Paulikas, V. Stamenkovic, N.M. Markovic, Enhancing hydrogen evolution activity in water splitting by Tailoring Li^+-$Ni(OH)_2$-Pt interfaces, Science 334 (2011) 1256–1260.
[41] E. Liu, J. Li, L. Jiao, H.T.T. Doan, Z. Liu, Z. Zhao, Y. Huang, K.M. Abraham, S. Mukerjee, Q. Jia, Unifying the hydrogen evolution and oxidation reactions kinetics in base by identifying the catalytic roles of hydroxyl-water-cation adducts, J. Am. Chem. Soc. 141 (2019) 3232–3239.
[42] F.J. Sarabia, P. Sebastián-Pascual, M.T.M. Koper, V. Climent, J.M. Feliu, Effect of the interfacial water structure on the hydrogen evolution reaction on Pt(111) modified with different nickel hydroxide coverages in alkaline media, ACS Appl. Mater. Interfaces 11 (2019) 613–623.
[43] W. Huang, H. Wang, J. Zhou, J. Wang, P.N. Duchesne, D. Muir, P. Zhang, N. Han, F. Zhao, M. Zeng, J. Zhong, C. Jin, Y. Li, S.-T. Lee, H. Dai, Highly active and durable methanol oxidation electrocatalyst based on the synergy of platinum–nickel hydroxide–graphene, Nat. Commun. 6 (2015) 10035.
[44] R. Artal, A. Serrà, J. Michler, L. Philippe, E. Gómez, Electrodeposition of mesoporous Ni-Rich Ni-Pt films for highly efficient methanol oxidation, Nanomaterials 10 (2020) 1435.
[45] R. Jamil, M. Sohail, N. Baig, M.S. Ansari, R. Ahmed, Synthesis of hollow Pt-Ni nanoboxes for highly efficient methanol oxidation, Sci. Rep. 9 (2019) 15273.
[46] J.L. Cohen, D.J. Volpe, H.D. Abruña, Electrochemical determination of activation energies for methanol oxidation on polycrystalline platinum in acidic and alkaline electrolytes, Phys. Chem. Chem. Phys. 9 (2007) 49–77.
[47] M. Li, K. Duanmu, C. Wan, T. Cheng, L. Zhang, S. Dai, W. Chen, Z. Zhao, P. Li, H. Fei, Y. Zhu, R. Yu, J. Luo, K. Zang, Z. Lin, M. Ding, J. Huang, H. Sun, J. Guo, X. Pan, W.A. Goddard, P. Sautet, Y. Huang, X. Duan, Single-atom tailoring of platinum nanocatalysts for high-performance multifunctional electrocatalysis, Nat. Catal. 2 (2019) 495–503.
[48] Q. Jiang, L. Jiang, H. Hou, J. Qi, S. Wang, G. Sun, Promoting effect of Ni in PtNi bimetallic electrocatalysts for the methanol oxidation reaction in alkaline media: experimental and density functional theory studies, J. Phys. Chem. C. 114 (2010) 19714–19722.
[49] I. Khalakhan, M. Vorokhta, P. Kúš, M. Dopita, M. Václavů, R. Fiala, N. Tsud, T. Skála, V. Matolín, In situ probing of magnetron sputtered Pt-Ni alloy fuel cell catalysts during accelerated durability test using EC-AFM, Electrochim. Acta 245 (2017) 760–769.
[50] I. Khalakhan, M. Vorokhta, X. Xie, L. Piliai, I. Matolínová, On the interpretation of X-ray photoelectron spectra of Pt-Cu bimetallic alloys, J. Electron Spectrosc. Relat. Phenom. 246 (2021), 147027.
[51] D. Fantauzzi, S. KrickCalderón, J.E. Mueller, M. Grabau, C. Papp, H.-P. Steinrück, T.P. Senftle, A.C.T. vanDuin, T. Jacob, Growth of stable surface oxides on Pt(111) at near-ambient pressures, Angew. Chem. Int. Ed. 56 (2017) 2594–2598.
[52] H. Yuan, J.-P. Li, F. Su, Z. Yan, B.T. Kusema, S. Streiff, Y. Huang, M. Pera-Titus, F. Shi, Reductive amination of furanic aldehydes in aqueous solution over versatile Ni_yAlO_x catalysts, ACS Omega 4 (2019) 2510–2516.
[53] L. Qiao, X. Bi, Direct observation of Ni^{3+} and Ni^{2+} in correlated $LaNiO_{3-\delta}$ films, Epl 93 (2011) 57002.
[54] S. Ghosh, M. Baral, R. Kamparath, S.D. Singh, T. Ganguli, Investigations on band commutativity at all oxide p-type NiO/n-type β-Ga_2O_3 heterojunction using photoelectron spectroscopy, Appl. Phys. Lett. 115 (2019), 251603.
[55] B.P. Payne, M.C. Biesinger, N.S. McIntyre, The study of polycrystalline nickel metal oxidation by water vapour, J. Electron Spectrosc. Relat. Phenom. 175 (2009) 55–65.
[56] S. Liu, J. Zong, Z.-J. Zhao, J. Gong, Exploring the initial oxidation of Pt, Pt3Ni, Pt3Au (111) surfaces: a genetic algorithm based global optimization with density functional theory, Green, Chem. Eng. 1 (2020) 56–62.
[57] R. Mu, X. Guo, Q. Fu, X. Bao, Oscillation of surface structure and reactivity of PtNi bimetallic catalysts with redox treatments at variable temperatures, J. Phys. Chem. C. 115 (2011) 20590–20595.
[58] F.U. Hillebrecht, J.C. Fuggle, P.A. Bennett, Z. Zołnierek, C. Freiburg, Electronic structure of Ni and Pd alloys. II. X-ray photoelectron core-level spectra, Phys. Rev. B. 27 (1983) 2179–2193.
[59] C. Zhang, X. Liang, R. Xu, C. Dai, B. Wu, G. Yu, B. Chen, X. Wang, N. Liu, H2 in situ inducing strategy on Pt surface segregation over low Pt Doped $PtNi_5$ nanoalloy with superhigh alkaline HER activity, Adv. Funct. Mater. 31 (2021) 2008298.
[60] M. Gong, Z. Deng, D. Xiao, L. Han, T. Zhao, Y. Lu, T. Shen, X. Liu, R. Lin, T. Huang, G. Zhou, H. Xin, D. Wang, One-nanometer-thick Pt_3Ni bimetallic alloy nanowires advanced oxygen reduction reaction: integrating multiple advantages into one catalyst, ACS Catal. 9 (2019) 4488–4494.